university of groningen

University Medical Center Groningen

University of Groningen

Analysis of a constant-coefficient pressure equation method for fast computations of two-phase flows at high density ratios

Cifani, Paolo

Published in:
Journal of computational physics

DOI:
10.1016/j.jcp.2019.108904

IMPORTANT NOTE: You are advised to consult the publisher's version (publisher's PDF) if you wish to cite from it. Please check the document version below.

Document Version
Publisher's PDF, also known as Version of record

Publication date:
2019

Link to publication in University of Groningen/UMCG research database

Citation for published version (APA):
Cifani, P. (2019). Analysis of a constant-coefficient pressure equation method for fast computations of two-phase flows at high density ratios. *Journal of computational physics*, *398*, [108904]. https://doi.org/10.1016/j.jcp.2019.108904

Copyright
Other than for strictly personal use, it is not permitted to download or to forward/distribute the text or part of it without the consent of the author(s) and/or copyright holder(s), unless the work is under an open content license (like Creative Commons).

The publication may also be distributed here under the terms of Article 25fa of the Dutch Copyright Act, indicated by the “Taverne” license. More information can be found on the University of Groningen website: https://www.rug.nl/library/open-access/self-archiving-pure/taverne-amendment.

Take-down policy
If you believe that this document breaches copyright please contact us providing details, and we will remove access to the work immediately and investigate your claim.

Downloaded from the University of Groningen/UMCG research database (Pure): http://www.rug.nl/research/portal. For technical reasons the number of authors shown on this cover page is limited to 10 maximum.

Journal of Computational Physics 398 (2019) 108904

Contents lists available at ScienceDirect

Journal of Computational Physics

www.elsevier.com/locate/jcp

Analysis of a constant-coefficient pressure equation method for fast computations of two-phase flows at high density ratios

Paolo Cifani

Computational Mechanics and Numerical Mathematics, University of Groningen, Nijenborgh 9, 9747 AG Groningen, the Netherlands

ARTICLE INFO

Article history:
Received 26 January 2019
Received in revised form 16 August 2019
Accepted 17 August 2019
Available online 23 August 2019

Keywords:
Modified constant-coefficient pressure equation
Projection method
Pressure jump
VOF
GFM
DNS Two-phase flows

ABSTRACT

An analysis of a modified pressure-correction formulation for fast simulations of fully resolved incompressible two-phase flows has been carried out. By splitting of the density weighted pressure gradient, the pressure equation is reduced to a constant-coefficient Poisson equation, for which efficient linear solvers can be used. While the gain in speed-up is well documented, the error introduced by the temporal extrapolation of the pressure gradient requires further investigations. In this paper it is shown that the modified pressure equation can lead to unphysical pressure oscillations and large errors. By appropriately combining the extrapolated pressure gradient with a matching volume fraction gradient grid convergence at high density ratios could be recovered. The cases of a one-dimensional front and a sphere translating at uniform velocity were first considered, allowing to decouple the pressure equation from the momentum equation. Subsequently, the case of a rising bubble in an upflow is analysed for which the full set of governing equations is solved. The pressure jump extrapolation error has been found dependent on the density ratio and the CFL number. Ultimately, the gain in the computational time, made possible by the use of fast Poisson solvers, should be weighted by the additional computational time the reduction of the aforementioned error may require.

© 2019 Elsevier Inc. All rights reserved.

1. Introduction

Immersed boundary (IB) methods for the tracking/capturing of fluid interfaces are widely used and among the most successful methods for the solution of the Navier-Stokes equations for finite Reynolds numbers [1]. The simple discretisation of the governing equations in a structured fixed-in-time grid and the computational efficiency derived from it represent neat advantages compared to body-fitted grid methods.

The common base ground of IB methods for fully resolved two-phase flows is the definition of a single set of governing equations, valid for the whole field, referred to as 'one-fluid' approach [1]. Rather than solving for two separate single-phase flow domains, the Navier-Stokes equations are modified by adding localised interface terms and differences in the material properties are accounted for. These two steps introduce important challenges to the discretisation of the governing equations, where one has to handle jumps in the fundamental variables (e.g. pressure) as well as the approximation of δ-functions on a finite-size computational grid (e.g. surface tension discretisation).

E-mail address: p.cifani@rug.nl.

https://doi.org/10.1016/j.jcp.2019.108904
0021-9991/© 2019 Elsevier Inc. All rights reserved.

The standard projection method [2], applied to the Navier-Stokes equations, leads to the following semi-discrete form of the pressure equation:

$$\nabla \cdot \left(\frac{1}{\rho} \nabla p \right) = \frac{1}{\alpha \Delta t} \nabla \cdot \mathbf{u}^*, \tag{1}$$

where p is the pressure, ρ is the density, $\mathbf{u}^*$ an intermediate non-solenoidal field, Δt the discrete time interval and α a coefficient that depends on the particular time integration scheme. The presence of discontinuous coefficients, in this case given by $1/\rho$, deteriorates the convergence of standard multigrid-based Poisson solvers [3] and the limitations are more severe the larger the density ratio. This has been a topic of research in the past years and several improvements have been suggested, some of which are summarised in [4]. These methods mainly focus on better interpolation operators for the transfer of data from fine to coarse grids (coarsening operators) and vice-versa (prolongation operators) in the presence of discontinuities. While this is certainly a viable option, an alternative, yet efficient strategy originally developed by Dong and Shen [5], and subsequently applied by Dodd and Ferrante [6], will be pursued. The idea is to split the density weighted pressure gradient into two contributions, one having a constant density weight and the other having a variable density weight. The latter is then approximated by extrapolation of the pressure gradient from previous time levels. This leads to the following modified pressure equation:

$$\nabla^2 p = \nabla \cdot \left[\left(1 - \frac{\rho_0}{\rho} \right) \nabla \hat{p} \right] + \nabla \cdot \left(\rho_0 \frac{\mathbf{u}^*}{\alpha \Delta t} \right), \tag{2}$$

where ρ_0 is a constant and $\nabla \hat{p}$ is an approximation of ∇p. In particular, in [6] a standard second order extrapolation in time is employed to evaluate $\nabla \hat{p}$:

$$\nabla \hat{p} = 2 \nabla p^n - \nabla p^{n-1}, \tag{3}$$

with n and $n-1$ the current and previous time level, respectively. Extrapolation (3) delivers a second order accurate ∇p for smooth pressure fields. However, the pressure may present discontinuities at the two-phase interface, as for example the pressure jump given by surface tension. An accurate discretisation of $\nabla \hat{p}$ appears then to be essential. Depending on the governing parameters and on the adopted discretisation methods, extrapolation (3) may lead to large numerical errors, the importance of which appears to have not been rigorously investigated so far.

The main goal of this work is to analyse the implication brought about by (3) and to quantify the error which arises from it. The result of this analysis will provide new insights into the numerical stability and accuracy of Eq. (2). This will constitute a guideline for the choice of the grid size and time step of the simulation. As it will become clear from this paper, Eq. (2), in the presence of jumps, can lead to unphysical oscillations of the pressure field for a moving two-phase interface. A discretisation of (3) based on the Ghost-Fluid-Method (GFM) [7], also employed in [8–10], will be shown able to mimic the essential numerical properties inherent of the unmodified pressure-correction formulation, delivering a substantially more accurate solution than that obtainable by a standard discretisation of (3).

The problem will be tackled by analysing a simplified one-dimensional model that retains all the relevant features of the full problem, showing the inconsistencies brought about by (3) and providing a general solution that can be easily embedded into the framework of standard multiphase solvers. Even though the considerations are derived from a Volume-of-Fluid (VOF) [11] standpoint, the results are general and applicable to other methods based on the 'one-fluid' approach, among which the Level-Set (LS) method [12], the Front-Tracking method [13] and combinations of these [14].

The paper is structured as follows: first, the mathematical model is described in Section 2. Following, the fractional step method for the unmodified, as well as for the modified pressure equation is detailed in Section 3. A one-dimensional test problem, characterised by a moving front at constant velocity, is then built and solved exactly in Subsection 3.2. This analytical solution is used as a reference for the validation of the discrete counterpart of the problem given by the unmodified pressure equation (1) and the modified pressure equation (2) in Sec. 3.2.2 and Sec. 3.2.4, respectively. The source of inconsistency in the original formulation used in [6] is investigated and an improved method, based on the GFM method [10] will be analysed in Sec. 3.2.5.

Next, the modified pressure-correction algorithm is tested first for a translating sphere at imposed flow (Sec. 4.1), where grid convergence is investigated for two different density ratios equal to 10 and 1000. Subsequently, the full set of governing equations is examined. In particular, the dependence of the pressure extrapolation error on the CFL number and on the density ratio is analysed for the case of a rising bubble in an upflow (Sec. 4.2).

The main findings and achievements are collected in Sec. 5.

2. Mathematical model

The incompressible Navier-Stokes equations for two immiscible fluids read [1]:

$$\rho \left[\frac{\partial \mathbf{u}}{\partial t} + \nabla \cdot (\mathbf{u}\mathbf{u}) \right] = -\nabla p + \nabla \cdot (2\mu \mathbf{D}) + \sigma k \mathbf{n} \delta(n), \tag{4}$$

$$\nabla \cdot \mathbf{u} = 0, \tag{5}$$

where $\mathbf{u}$ is the velocity, ρ is the density, μ is the dynamic viscosity, σ is the surface tension coefficient, k is the curvature, $\mathbf{n}$ is the normal vector to the interface, $\mathbf{D}$ is the deformation tensor and δ is the Dirac function which localises the surface tension at the interface [15]. The spatial distribution of the two phases is defined by a marker function f, equal to 1 in the gas phase and equal to 0 in the liquid phase. Function f, being the volume fraction field in the VOF method, is transported by the underlying velocity field as follows:

$$\frac{\partial f}{\partial t} + \mathbf{u} \cdot \nabla f = 0. \tag{6}$$

Density and dynamic viscosity are then derived from the marker function as:

$$\begin{aligned} \rho &= \rho_l(1-f) + \rho_g f, \\ \mu &= \mu_l(1-f) + \mu_g f, \end{aligned} \tag{7}$$

where ρ_l, ρ_g and μ_l, μ_g are the density and the dynamic viscosity of the liquid phase and the gas phase, respectively. In turn, expressions (7) couple f to the Navier-Stokes equations.

3. Numerical algorithm

3.1. Modified pressure-correction formulation

The temporal and spatial discretisation of Eqs. (4), (5) and (6) is described in details in [16]. For completeness, here the steps of the projection method [2] for two-phase flows are reported, which will be used for the derivations carried out in the following sections. The main concepts that will be presented in this work are independent of the particular time marching scheme adopted for the momentum equation (4). Without loss of generality, the Euler forward scheme will be used to illustrate the numerical properties of the algorithm.

At the beginning of each time level n, Eq. (6) is solved by employing a piece-wise linear reconstruction of the interface and a geometric evaluation of the volume fraction fluxes [17], delivering f at time level $n+1$. Density and dynamic viscosity are then updated through (7), and the surface tension term at time level $n+1$ is computed. The latter requires the computation of curvature, for which the Generalised Height Function (GHF) method is used [18,16]. At this point, a non-solenoidal vector field $\mathbf{u}^*$ can be evaluated from:

$$\frac{\mathbf{u}^* - \mathbf{u}^n}{\Delta t} + (\mathcal{C}^n - \mathcal{V}^n)\mathbf{u}^n = \left(\frac{\sigma k}{\rho}\mathcal{G}f\right)^{n+1}, \tag{8}$$

where $\mathcal{C}$ is the discrete convection operator $u \cdot \nabla$, $\mathcal{V}$ is the discrete diffusion operator $\frac{1}{\rho^{n+1}}\nabla \cdot \left(2\mu^{n+1}\nabla\right)$ and $\mathcal{G}$ the discrete gradient operator ∇. The surface tension term is mapped onto the Eulerian grid through the volume fraction gradient [18]. The continuity constraint (5) results in the discrete Poisson equation

$$\mathcal{D}\left(\frac{1}{\rho^{n+1}}\mathcal{G}p^{n+1}\right) = \mathcal{D}\left(\frac{\mathbf{u}^*}{\Delta t}\right), \tag{9}$$

where $\mathcal{D}$ is the discrete divergence operator $\nabla\cdot$. The velocity at the new time level is then obtained using the following relation

$$\mathbf{u}^{n+1} = \mathbf{u}^* - \Delta t\left(\frac{1}{\rho^{n+1}}\mathcal{G}p^{n+1}\right), \tag{10}$$

delivering a numerically divergence-free velocity field.

Eq. (9) involves the solution of a Poisson equation with discontinuous coefficients. This has been shown to lead to performance problems for standard Poisson solvers [4]. A modified constant-coefficient Poisson equation can be derived instead [5,6], which allows for the use of fast Poisson solvers. The density weighted pressure gradient is split into two contributions:

$$\frac{1}{\rho^{n+1}}\nabla p^{n+1} \approx \frac{1}{\rho_0}\nabla p^{n+1} + \left(\frac{1}{\rho^{n+1}} - \frac{1}{\rho_0}\right)\nabla \hat{p}, \tag{11}$$

where ρ_0 is a constant. Using the same notation as in [6], the pressure gradient $\nabla\hat{p}$ represents an approximation of ∇p^{n+1}. As already noted in [6], a first order approximation of the pressure gradient leads to large errors. For this reason, throughout the rest of this paper, only the second order extrapolation (3) will be considered. Substituting (11) into (9) and multiplying by ρ_0 the modified constant-coefficient Poisson equation is found:

$$\mathcal{D}\left(\mathcal{G}p^{n+1}\right) = \mathcal{D}\left[\left(1 - \frac{\rho_0}{\rho^{n+1}}\right)\mathcal{G}\hat{p}\right] + \mathcal{D}\left(\rho_0\frac{\mathbf{u}^*}{\Delta t}\right). \tag{12}$$

Finally, the corresponding velocity correction can be found by substituting (11) into (10), obtaining a numerical divergence-free velocity:

$$\mathbf{u}^{n+1} = \mathbf{u}^{*} - \Delta t \left[\frac{1}{\rho_0} \mathcal{G} p^{n+1} + \left(\frac{1}{\rho^{n+1}} - \frac{1}{\rho_0} \right) \mathcal{G} \hat{p} \right]. \tag{13}$$

Summarising, the modifications to implement in the projection method for the solution of the Navier-Stokes equations, involving only a constant-coefficient pressure equation, are the use of (12) instead of (9) and the use of (13) instead of (10). The Poisson matrix of (12) reduces to a standard constant-coefficients matrix, for which several efficient solvers, iterative and direct, are available from single-phase flow studies. However, given the presence of pressure discontinuities particular care should be taken in the extrapolation of $\mathcal{G}\hat{p}$, in order to avoid large numerical errors. This will be the subject of interest of the following sections, where the modified pressure-correction formulation will be analysed and subsequently tested for kinematic and dynamic test cases.

3.2. One-dimensional analysis of a moving front

In order to illustrate the implications brought about by (11), a one-dimensional model which retains all the relevant features of the full problem (4)–(7) will be built and analysed. First, in Sec. 3.2.1, the latter problem will be solved analytically. Subsequently, in Sec. 3.2.2 and Sec. 3.2.4 the unmodified pressure-correction formulation (8)–(10) and the modified pressure-correction formulation (8), (12), (13) will be used to obtain a numerical solution of the same problem. The result of the analysis will show how, by appropriately combining the pressure gradient with the volume fraction gradient, the exact solution for this problem can be recovered (Sec. 3.2.5).

3.2.1. Exact solution

Consider the following problem:

$$\frac{\partial u}{\partial t} = \frac{1}{\rho} \left(-\frac{dp}{dx} + \frac{df}{dx} \right), \tag{14}$$

$$\frac{du}{dx} = 0, \tag{15}$$

for $x \in (0, L)$, subject to the initial condition $u(x, 0) = U$ and to the boundary conditions $u(x = 0, t) = u(x = L, t) = U$; $(dp/dx)\,|_{x=0,t} = (dp/dx)\,|_{x=L,t} = 0$. The indicator function f is defined as:

$$f(x, t) = \begin{cases} 0, & \text{if } x < x_s \\ 1, & \text{if } x \geq x_s \end{cases} \tag{16}$$

where x_s is the position of a moving interface at velocity u. The second term in the right-hand-side of (14) is a one-dimensional equivalent of the surface tension term, which is, effectively, a δ-function at the interface. Eq. (15) imposes $u(x, t) = U$, hence from Eq. (14) it follows that the pressure gradient has to equal the volume fraction gradient. Furthermore, bearing in mind the boundary conditions, the analytical solution is found:

$$p(x, t) = f(x, t) + p_0, \tag{17}$$

with p_0 an arbitrary reference pressure.

In Sec. 3.2.2 and Sec. 3.2.4 problem (14)–(15) will be solved numerically by employing the unmodified and the modified pressure-correction formulation, respectively.

3.2.2. Numerical solution: unmodified pressure-correction formulation

Problem (14)–(15) is discretised on a uniform and staggered grid of spacing Δx (Fig. 1). Let N be the number of cells. The positions of the collocated points are indicated by whole integers and defined as $x_{c,i} = (i - 1/2)\,\Delta x$ for $i = 1, \ldots, N$. Given a position $x_{c,i}$, the positions of its neighbouring staggered points are indicated by half-integers and defined as $x_{s,i\pm1/2} = x_{c,i} \pm \Delta x/2$. The discretisation of the operators $\mathcal{G}$ and $\mathcal{D}$ is as such that the two operators are each other adjoint [19]:

$$\begin{aligned} \mathcal{G}_{i+1/2}(q) &= \frac{q_{i+1} - q_i}{\Delta x}, \qquad i = 0, \ldots, N \\ \mathcal{D}_i(w) &= \frac{w_{i+1/2} - w_{i-1/2}}{\Delta x}, \quad i = 1, \ldots, N \end{aligned} \tag{18}$$

with q and w two generic discrete quantities defined on the collocated nodes and on the staggered nodes, respectively. In particular, the velocity field will be defined at the staggered grid locations while the pressure and volume fraction field will be defined at the collocated grid locations. Homogeneous Neumann boundary conditions are applied at the boundaries. Furthermore, the indicator function f is advected exactly by solving analytically Eq. (6).

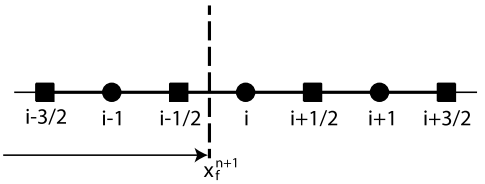

Fig. 1. Sketcth of a one-dimensional stencil. The interface is located between nodes $i-1/2$ and i at time level $n+1$.

Consider an interface located between nodes $i-1/2$ and i at time level $n+1$, as depicted in Fig. 1. The position of the front x_f is advected analytically and so is the corresponding density field through Eq. (7). From (8), u^* is evaluated:

$$u_s^* = \begin{cases} U + \frac{\Delta t}{\rho_s^{n+1}} \mathcal{G}_s f^{n+1}, & s = i-1/2 \\ U, & \text{otherwise} \end{cases} \tag{19}$$

where U is a constant velocity. The unmodified pressure equation (9) yields:

$$\begin{aligned} \mathcal{D}_j \left(\frac{1}{\rho^{n+1}} \mathcal{G} p^{n+1} \right) &= \frac{1}{\rho_{i-1/2}^{n+1} \Delta x} \mathcal{G}_{i-1/2} f^{n+1}, && j = i-1 \\ \mathcal{D}_j \left(\frac{1}{\rho^{n+1}} \mathcal{G} p^{n+1} \right) &= -\frac{1}{\rho_{i-1/2}^{n+1} \Delta x} \mathcal{G}_{i-1/2} f^{n+1}, && j = i \\ \mathcal{D}_j \left(\frac{1}{\rho^{n+1}} \mathcal{G} p^{n+1} \right) &= 0. && \text{otherwise} \end{aligned} \tag{20}$$

It is straightforward to verify that the following expression is the solution to system (20):

$$p_i^{n+1} = \begin{cases} p_0, & \text{if } x_i < x_f \\ p_0 + \Delta f, & \text{if } x_i \geq x_f \end{cases} \tag{21}$$

where Δf is the difference between the value of f on the right side and on the left side of the front. Finally, velocity correction (10) results in

$$u_s^{n+1} = \begin{cases} u_s^* - \frac{\Delta t}{\rho_s^{n+1}} \mathcal{G}_s p^{n+1}, & s = i-1/2 \\ U, & \text{otherwise} \end{cases} \tag{22}$$

Substituting (19) and (21) into (22) yields:

$$u_s^{n+1} = U, \quad \forall\, s \tag{23}$$

which satisfies the continuity constraint (15). Hence, the unmodified pressure-correction formulation is able to recover the exact solution (17). Note that, in order to arrive at solution (21), (23), it was assumed to employ the same operator $\mathcal{G}$ for the discretisation of the pressure gradient and the indicator function gradient. When this condition is verified, an exact numerical balance of the terms in the RHS of (14) can be achieved [20].

In the next subsection the numerical stability of the modified pressure equation will be investigated. Subsequently, in Sec. 3.2.4 problem (14)–(15) will be solved numerically by employing the modified pressure-correction formulation.

3.2.3. Stability analysis of the modified pressure equation

As a preliminary step in deriving a discrete solution of system (14)–(15) by applying the modified pressure equation (12), the numerical stability of the latter will be analysed. A formal Fourier stability analysis is not applicable to Eq. (12) given the presence of the discontinuous coefficients ρ_0/ρ^{n+1}. However, if one considers the following simplified equation: only the first term on the right-hand side of (12) is relevant for stability since it explicitly contains the variable p; the density ρ^{n+1} is assumed to be constant with values $\overline{\rho} = \rho_l$ or $\overline{\rho} = \rho_g$; then the amplification factor can be found as follows. First, by defining the constant $\eta = 1 - \rho_0/\overline{\rho}$, Eq. (12) is rewritten as

$$\mathcal{L} p^{n+1} - \eta \mathcal{L} \left(2p^n - p^{n-1} \right) = 0, \tag{24}$$

with $\mathcal{L} = \mathcal{D}\mathcal{G}$ the discrete Laplacian. Secondly, by placing $p^n = \xi^n p^0$ in Eq. (24), the characteristic equation can be easily found:

$$\xi^2 - 2\eta\xi + \eta = 0. \tag{25}$$

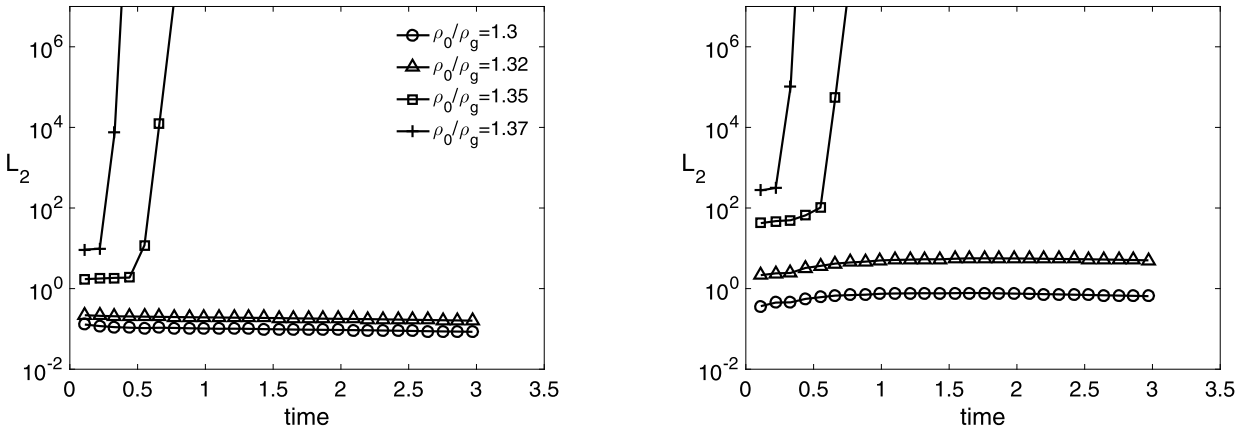

Fig. 2. L_2 norm of the pressure error as a function of time for problem (14)–(15) using the modified pressure-correction formulation. A number of values of ρ_0/ρ_g around the theoretical stability boundary have been simulated, as indicated in the legend. The left figure refers to $\rho_l/\rho_g = 10$, the right figure refers to $\rho_l/\rho_g = 1000$.

The roots of the stability polynomial (25) are $\xi_1 = \eta + \sqrt{\eta^2 - \eta}$, $\xi_2 = \eta - \sqrt{\eta^2 - \eta}$, hence (24) is stable if the following conditions are verified:

$$\left|\eta \pm \sqrt{\eta^2 - \eta}\right| \leq 1 \iff -\frac{1}{3} \leq \eta \leq 1, \tag{26}$$

which results in the stability restriction

$$0 < \rho_0 \leq \frac{4}{3}\rho_g, \tag{27}$$

with ρ_g being the smallest density value. Inequality (27) has been numerically tested for the problem defined in Sec. 3.2.1. In particular, a front moving at velocity $U = 1$ has been considered and simulated for two density ratios $\rho_l/\rho_g = 10, 1000$ at CFL=0.05. Fig. 2 shows the L_2 norm of the pressure error as a function of time for values of ρ_0/ρ_g around the boundary $\rho_0/\rho_g = 4/3$. In spite of the simplifying assumptions made in the stability analysis, restriction (27) well predicts the stability boundary independently of the density ratio. Note that, large errors are found also for the stable simulations at high density ratios. The source of this numerical error will be explained in detail in Sec. 3.2.4. Furthermore, in Sec. 3.2.5 an improved pressure-correction formulation, able to recover the exact solution for this problem, will be presented.

Finally, next to the stability condition (27) the truncation error of extrapolation (3) can be considered for the choice of ρ_0. In particular, assuming smoothness, the Taylor expansion of p^{n+1} around time level n and $n-1$ yields the truncation error

$$\tau = \left(\frac{1}{\rho} - \frac{1}{\rho_0}\right) \nabla \left[-\frac{\partial^2 p}{\partial t^2}\bigg|^n \Delta t^2 + \mathcal{O}(\Delta t^3) \right]. \tag{28}$$

For a given Δt and density field, error (28) increases as $\rho_0 \to 0$. Bearing in mind stability restriction (27), ρ_0 is set equal to ρ_g. This is also the choice in the works [6,16] and will be adopted throughout the rest of this paper.

In the following section the one-dimensional problem (14)–(15) will be solved numerically by employing the modified pressure-correction formulation.

3.2.4. Numerical solution: modified pressure-correction formulation

Differently from the derivation carried out in Sec. 3.2.2, the position of the interface at different time levels has to be considered in order to take into account the terms introduced by (3). Consider the situation depicted in Fig. 3. An interface moves through the computational grid, occupying the positions indicated by the dashed lines, at time levels $n-1$, n and $n+1$. First, a non-solenoidal velocity is evaluated as in (19). Subsequently, the modified Poisson equation (12) yields:

$$\begin{aligned}
\mathcal{D}_j\left(\mathcal{G}p^{n+1}\right) &= \mathcal{D}_j\left[\left(1 - \frac{\rho_0}{\rho^{n+1}}\right)\left(2\mathcal{G}p^n - \mathcal{G}p^{n-1}\right)\right] + \frac{\rho_0}{\rho^{n+1}_{i+1/2}\Delta x}\mathcal{G}_{i+1/2}f^{n+1}, \qquad j = i \\
\mathcal{D}_j\left(\mathcal{G}p^{n+1}\right) &= \mathcal{D}_j\left[\left(1 - \frac{\rho_0}{\rho^{n+1}}\right)\left(2\mathcal{G}p^n - \mathcal{G}p^{n-1}\right)\right] - \frac{\rho_0}{\rho^{n+1}_{i+1/2}\Delta x}\mathcal{G}_{i+1/2}f^{n+1}, \quad j = i+1 \\
\mathcal{D}_j\left(\mathcal{G}p^{n+1}\right) &= \mathcal{D}_j\left[\left(1 - \frac{\rho_0}{\rho^{n+1}}\right)\left(2\mathcal{G}p^n - \mathcal{G}p^{n-1}\right)\right]. \qquad \text{otherwise}
\end{aligned} \tag{29}$$

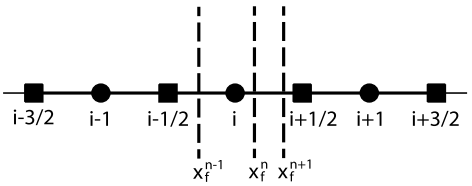

Fig. 3. Sketcth of a one-dimensional stencil. The interface positions at time level $n-1$, n and $n+1$ are depicted.

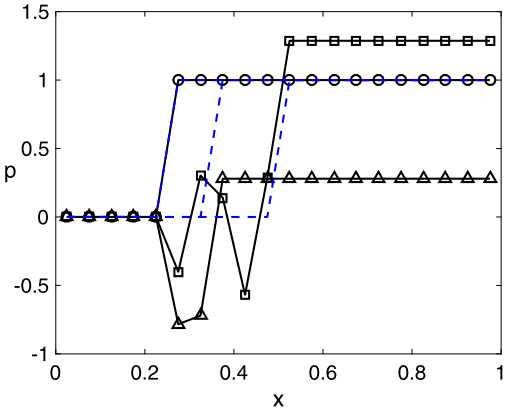

Fig. 4. Pressure field for problem (14)–(15) using the modified pressure-correction formulation at different time levels: $t=0$ (black line with circles); $t=0.125$ (black line with triangles); $t=0.25$ (black line with squares). The corresponding exact solution is represented by the dashed blue lines. The reference pressure p_0 is set to 0. (For interpretation of the colours in the figure(s), the reader is referred to the web version of this article.)

The pressure at the previous time levels p^{n-1} and p^n is assumed to be exact, so that $\mathcal{G}p^{n-1}=\mathcal{G}f^{n-1}$ and $\mathcal{G}p^n=\mathcal{G}f^n$. Eq. (29) leads then to

$$\begin{aligned}
&\mathcal{D}_j(\mathcal{G}p^{n+1}) = -\left(1-\frac{\rho_0}{\rho^{n+1}_{i-1/2}}\right)\frac{\mathcal{G}_{i-1/2}f^{n-1}}{\Delta x}, && j=i-1\\
&\mathcal{D}_j(\mathcal{G}p^{n+1}) = 2\left(1-\frac{\rho_0}{\rho^{n+1}_{i+1/2}}\right)\frac{\mathcal{G}_{i+1/2}f^{n}}{\Delta x}+\left(1-\frac{\rho_0}{\rho^{n+1}_{i-1/2}}\right)\frac{\mathcal{G}_{i-1/2}f^{n-1}}{\Delta x}+\frac{\rho_0}{\rho^{n+1}_{i+1/2}}\frac{\mathcal{G}_{i+1/2}f^{n+1}}{\Delta x}, && j=i\\
&\mathcal{D}_j(\mathcal{G}p^{n+1}) = -2\left(1-\frac{\rho_0}{\rho^{n+1}_{i+1/2}}\right)\frac{\mathcal{G}_{i+1/2}f^{n}}{\Delta x}-\frac{\rho_0}{\rho^{n+1}_{i+1/2}}\frac{\mathcal{G}_{i+1/2}f^{n+1}}{\Delta x}, && j=i+1\\
&\mathcal{D}_j(\mathcal{G}p^{n+1}) = 0. && \text{otherwise}
\end{aligned} \tag{30}$$

Following the same procedure used to solve system (20), the pressure field is derived:

$$p_j^{n+1}=\begin{cases} p_0, & j=1,\ldots,i-1\\ \Delta f\left(\frac{\rho_g}{\rho_l}-1\right)+p_0, & j=i\\ \Delta f\frac{\rho_g}{\rho_l}+p_0, & j=i+1\\ p_{i+1}. & j=i+2,\ldots,N\end{cases} \tag{31}$$

Note that, in Eqs. (31), ρ_0 has been placed equal to ρ_g as discussed in the stability analysis carried out in Sec. 3.2.3. From (31) it can be deduced that, while the pressure difference $p_{i+1}-p_i$ across the interface equals the exact jump Δf, the pressure value behind the front shows an unphysical negative oscillation, which tends to $-\Delta f$ as $\rho_g/\rho_l\to 0$. It is worth stressing that (31) is the solution of only the particular case depicted in Fig. 3. In fact, there are several configurations of the interface positions, on the computational grid, for which p assumes different values of those given by (31) including the exact solution. However, the case worked out above will always occur for a moving interface, independently of the CFL number and of the initial conditions. In other words, at some point in the time evolution, numerical wiggles in the pressure field will appear.

In Fig. 4 the evolution of the pressure profile is shown. A front moving from left to right at velocity $U=1$ in a domain of length 1 is considered. The density ratio is $\rho_l/\rho_g=100$ and the CFL number is 0.05. Starting from the exact solution at $t=0$, the pressure develops wiggles behind the front, as predicted from the above analysis.

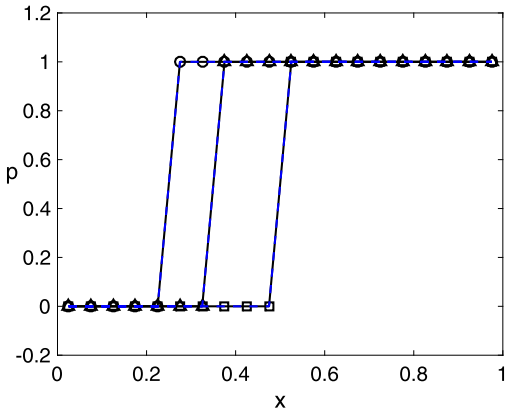

Fig. 5. Pressure field for problem (14)–(15) using the improved pressure-correction formulation at different time levels: $t = 0$ (black line with circles); $t = 0.125$ (black line with triangles); $t = 0.25$ (black line with squares). The corresponding exact solution is represented by the dashed blue lines. The reference pressure p_0 is set to 0.

In the next section an improved pressure-correction formulation based on the Ghost-Fluid-Method, also employed in [10], will be illustrated and tested for the same one-dimensional problem (14), (15).

3.2.5. An improved pressure-correction formulation

The origin of the unphysical pressure oscillations shown in Sec. 3.2.4 can be traced back to a poor approximation of the pressure jump condition when computing $\nabla\hat{p}$ from (3). In order to accurately evaluate the pressure gradient at the interface, the latter must be combined with the volume fraction gradient in the following way:

$$\mathcal{G}p - \sigma k \mathcal{G}f. \tag{32}$$

By doing so, an exact balance between the pressure and surface tension can be achieved, provided $k = \text{const}$ [20,21]. Relation (32) has to be then applied to every instance of the pressure gradient in the governing equations, including to $\mathcal{G}\hat{p}$. The surface tension is thus explicitly accounted for in the computation of the pressure gradient, as in the Ghost-Fluid-Method (GFM) [7–10], rather than a source term in the RHS of the momentum equation. Ultimately, this is a salient feature to design a more accurate pressure-correction formulation that makes use of a constant-coefficient Poisson equation through temporal extrapolation of the pressure gradient.

Based on the above reasoning, first Eq. (8) is evaluated not accounting, at this stage, for the contribution of the surface tension [22]:

$$\bar{\mathbf{u}}^* = \mathbf{u}^n - \Delta t(\mathcal{C}^n - \mathcal{V}^n)\mathbf{u}^n. \tag{33}$$

Then, using (32), Eq. (12) is rewritten as:

$$\mathcal{D}\left[\mathcal{G}p^{n+1} - (\sigma k \mathcal{G}f)^{n+1}\right] = \mathcal{D}\left[\left(1 - \frac{\rho_0}{\rho^{n+1}}\right)\left(\mathcal{G}\hat{p} - \widehat{\sigma k \mathcal{G}f}\right)\right] + \mathcal{D}\left(\rho_0 \frac{\bar{\mathbf{u}}^*}{\Delta t}\right), \tag{34}$$

where $\widehat{\sigma k \mathcal{G}f}$ represents the term $(\sigma k \mathcal{G}f)$ extrapolated from previous time levels according to the same time extrapolation used for $\mathcal{G}\hat{p}$. Note that $\left(\mathcal{G}\hat{p} - \widehat{\sigma k \mathcal{G}f}\right)$ constitutes an approximation of the smooth part of the extrapolated pressure gradient. This contribution can be consistently extrapolated using Eq. (3), which assumes smoothness. Finally, a divergence-free velocity field is constructed by substituting (32) into (13):

$$\mathbf{u}^{n+1} = \bar{\mathbf{u}}^* - \Delta t\left[\frac{1}{\rho_0}\left(\mathcal{G}p^{n+1} - (\sigma k \mathcal{G}f)^{n+1}\right) + \left(\frac{1}{\rho^{n+1}} - \frac{1}{\rho_0}\right)\left(\mathcal{G}\hat{p} - \widehat{\sigma k \mathcal{G}f}\right)\right]. \tag{35}$$

For the case of the one-dimensional moving front analysed in Sec. 3.2.1, the smooth part of the pressure gradient is zero since the pressure is constant on both sides of the interface. This condition is numerically satisfied by the combined gradient (32), so that the RHS of (34) is identically zero. Moreover, noting that for this particular problem σk is constant and equal to 1, Eq. (34) is equivalent to Eq. (9). The improved pressure-correction formulation is then able to deliver the exact solution (17). This has been numerically verified for the same case of a moving front at constant velocity U simulated in Sec. 3.2.4. The results of this test are shown in Fig. 5. Clearly, the exact solution is obtained.

The discontinuity in the viscosity field introduces an additional jump in pressure [1,22], which can be incorporated into (32) in a similar way to what has been done for the surface tension. In this paper μ is smoothed over three computational cells around the interface [18,10], thus regularising its contribution to the pressure gradient. Finally, it is worth noting that

the density weighted pressure gradient is continuous across the two-phase interface, provided the acceleration is continuous [10].

In the next section the accuracy of the modified and of the improved pressure-correction formulations will be tested for a set of three-dimensional test cases, both for an imposed flow (Sec. 4.1) as well as for the case of a rising bubble in an upflow (Sec. 4.2).

4. Three-dimensional results

In this section a number of three-dimensional test cases will be analysed in order to investigate the accuracy of the modified pressure-correction formulation (8), (12), (13) with respect to the that of the improved pressure-correction formulation (33), (34), (35). First a translating sphere will be considered. Pressure equations (12) and (34) will be solved for, while imposing a uniform velocity field. Differently from the one-dimensional problem (14)–(15), higher dimensional problems are characterised by a non-constant curvature. This is true, numerically, also for the case of a sphere due to the errors in the computation of k. In particular, here the curvature is computed by using the GHF method [18,16] having accuracy $\mathcal{O}(\Delta x^2)$. As a result, the pressure gradient does not balance the surface tension exactly. The latter observation can be concisely illustrated by recasting the relation (32) as follows:

$$\mathcal{G}p - \sigma k \mathcal{G} f = \mathcal{G}\left(p - \sigma k f\right) + \sigma f \mathcal{G} k. \tag{36}$$

The second term in the RHS of expression (36) will be, in general, different from zero since $k \neq$ const. Hence, even in the case in which $p = \sigma k f$ an exact balance will not be recovered. This aspect will be examined in Sec. 4.1. Subsequently, the full set of governing equations will be analysed for the case of a rising bubble in an upflow (Sec. 4.2).

For the rest of the paper the pressure obtained by using the modified pressure-correction formulation will be indicated by p^{mod}, while the pressure obtained by the improved pressure-correction formulation will be indicated by p^*.

4.1. Translating sphere

In this section a kinematic test case, representing a three-dimensional analogue of the problem (14)–(15), is investigated. A sphere translates within a periodic cubic domain of length 1 at constant velocity $U = 1$ along the x-axis. Based on the exact trajectory of the centre of the sphere, the volume fraction field is re-initialised each time step with a local grid refinement procedure, as described in [23]. Hence, with assigned $\mathbf{u}$ and f, pressure is the only variable being solved for.

Two density ratios $r = \rho_l/\rho_g$ are investigated, namely $r_{10} = 10$ and $r_{1000} = 1000$, with ρ_g and ρ_l the density inside and outside the sphere, respectively. The radius of the sphere R is equal to 0.25 and the surface tension coefficient σ is equal to 1. The exact pressure jump σk_{ex} is then equal to 8, where k_{ex} is the exact curvature. The reference solution used to estimate the pressure field error is defined as $p_{ref} = \sigma k_{ex} f$. This definition is independent of the initialisation procedure employed for f, highlighting only the part of the error due to the different pressure-correction formulations. The total simulation time T is such that the sphere completes one cycle through the domain.

A grid refinement study is conducted on 4 grid resolutions, starting from the coarse grid g_1 of 16^3 computational points and subsequently doubling the resolution along each direction up to 128^3 computational points for grid g_4. The CFL number is set to 0.08 for all simulated grids. The influence of the CFL number will be investigated later in this section and presented in Fig. 9. A qualitative result is shown in Fig. 6 for grid g_3 at $t = T/5$, after the sphere has moved from the centre of the domain towards the boundary $x = 1$. In the left figures p^{mod} is shown, while in the right figures p^* is shown. The top figures refer to density ratio r_{10}, the bottom figures refer to density ratio r_{1000}. Pressure p^{mod} shows spurious oscillations, which largely increase with the density ratio. On the contrary, p^* adheres closely to the reference solution for both density ratios.

In Fig. 7 the pressure profiles along the centre line aligned with the x-axis are shown for the investigated grid resolutions, at $t = T$. Convergence to the reference solution is qualitatively observed for p^* (right figures) both for r_{10} (top figure) and r_{1000} (bottom figure). The wiggles present in the p^{mod} profiles have amplitude increasing with the density ratio independently of the grid size.

The error in the pressure field is quantitatively measured by the L_2 norm

$$L_2 = \sqrt{\frac{1}{N}\sum_{i}^{N} |p_i - p_{i,ref}|^2}, \tag{37}$$

with N the total number of grid points. Error (37) is shown in Fig. 8. The blue lines are the results for p^*, while the red lines are the results for p^{mod}. The circles refer to r_{10} and the triangles refer to r_{1000}. Pressure p^* shows second order convergence toward the finer grid resolutions. The improved pressure-correction formulation makes use of the smooth pressure gradient (32) thus, the error related to the pressure extrapolation is expected to closely match the truncation error (28). The latter is found to be negligible with respect to the spatial truncation error of the pressure equation (34). For this particular test case, in fact, all the derivatives in the term between brackets of (28) are zero when evaluated at each side of the interface since

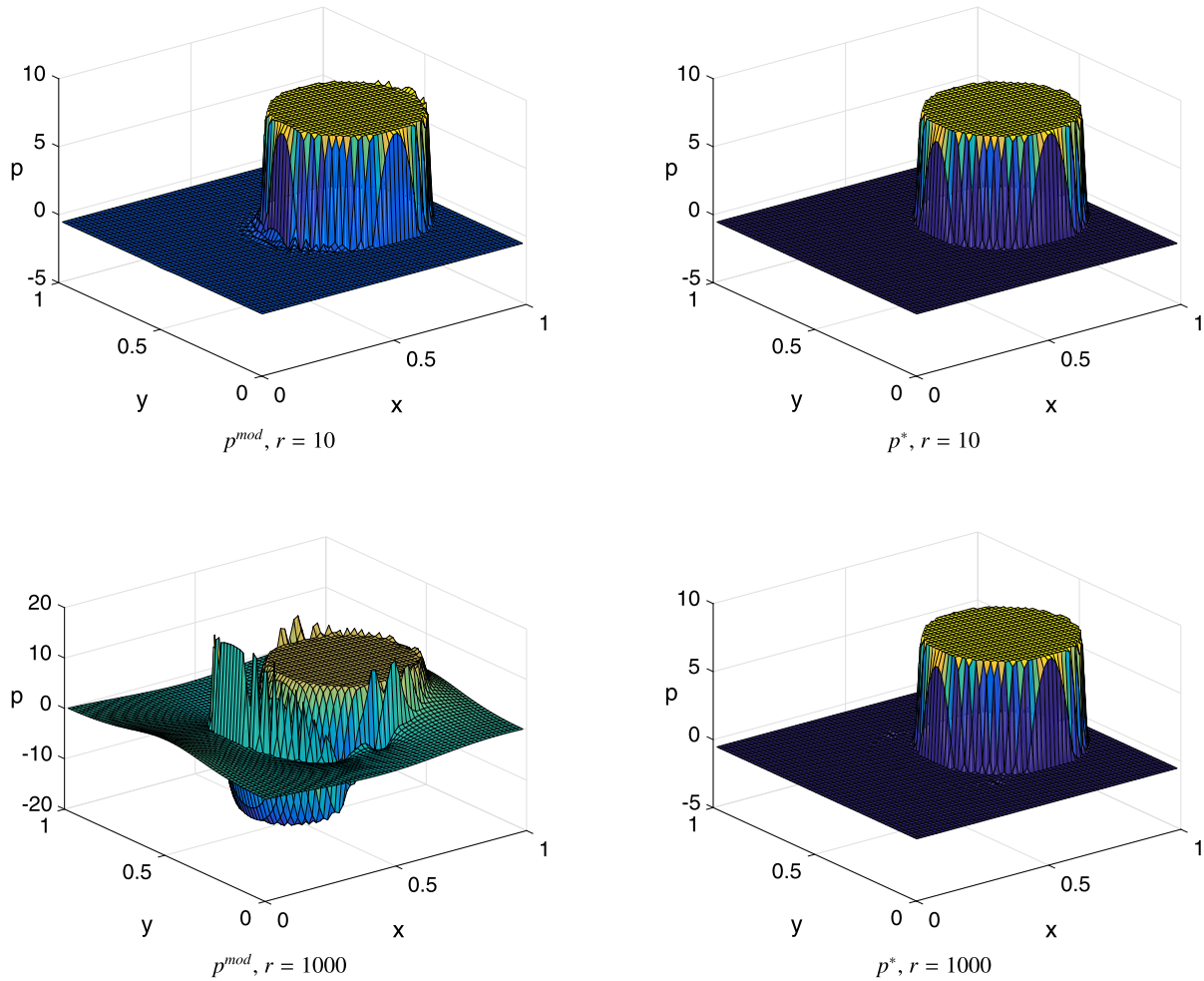

Fig. 6. Pressure profile in a mid-plane for grid g_3 at $t = T/5$: p^{mod} (left-column figures); p^* (right-column figures). The top figures refer to r_{10}, the bottom figures refer to r_{1000}.

p is constant. This is well represented by the L_2 norm of the error of p^*, which results to be approximately independent of the density ratio. In contrast, p^{mod} shows close to first order convergence for r_{10} and fails to converge for r_{1000} with an error about two orders of magnitude higher than that at the lower density ratio.

As argued in Sec. 3.2, the inconsistency in the discretisation of Eq. (12) does not vanish with decreasing CFL numbers. This was tested for grid g_3 starting from CFL= 0.32, and halving the time-step until CFL=0.04. Fig. 9 shows the pressure profiles along x for p^{mod} (left figure) and for p^* (right figure). The former shows spurious oscillations of approximately constant amplitude and increasing frequency, while p^* closely matches the reference solution for all simulated CFL. This supports the findings of Sec. 3.2 and shows that by employing the improved pressure-correction formulation an essentially wiggle-free solution can be achieved.

In the next section, the case of a rising bubble in an initially uniform flow will be investigated.

4.2. 3D buoyant bubble in a uniform upflow

In this section the modified pressure-correction formulation and the improved pressure-correction formulation will be tested for the case of a rising bubble in a uniform upflow. The full set of governing equations is solved. A second order Adams-Bashforth (AB2) scheme [24] is used for the temporal discretisation of the momentum equation and central finite differences are employed for the discretisation of the spatial derivatives.

The results presented in Sec. 4.1 are strictly valid for a uniform velocity field. For a non-trivial **u**, as that of a rising bubble, the second term in the RHS of Eq. (12) introduces additional contributions to p, which are carried over from Eq. (8). Furthermore, while in the translating cases examined in the previous sections f was imposed, here Eq. (6) is numerically solved for introducing yet another source of error. It becomes then of interest to quantify the importance of the pressure extrapolation error for such a more complex problem. To this aim, a set of test cases has been carried out for

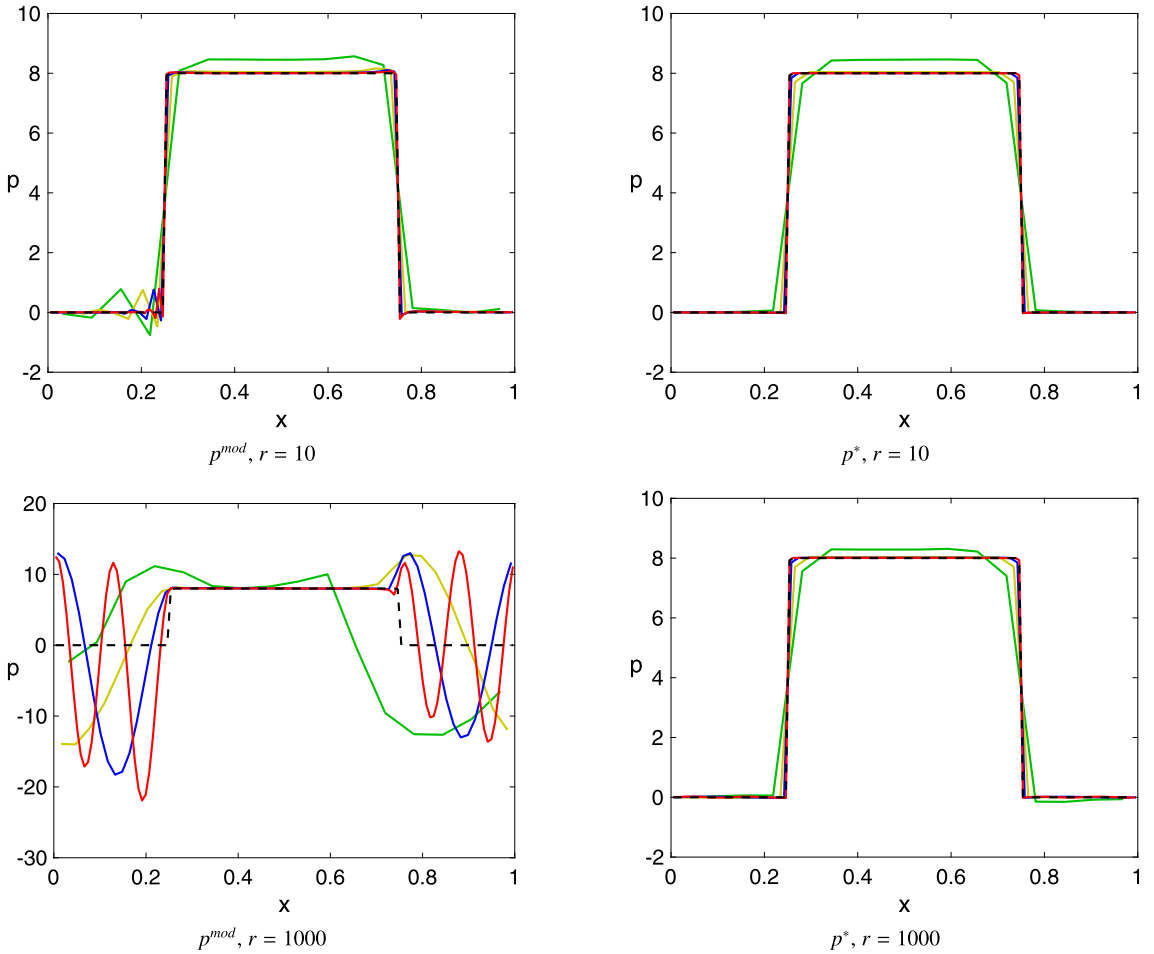

Fig. 7. Pressure profile in the centre line aligned with the x-axis for grid g_1 (green line), g_2 (dark yellow line), g_3 (blue line), g_4 (red line) at $t = T$: p^{mod} (left-column figures); p^* (right-column figures). The reference solution on the finest grid is shown by the dashed black line. The top figures refer to r_{10}, the bottom figures refer to r_{1000}.

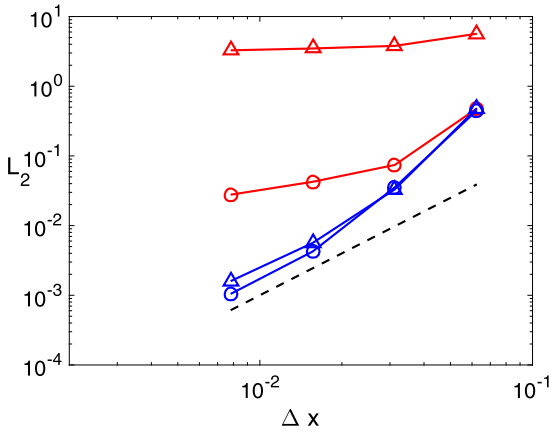

Fig. 8. L_2 norm (37) at $t = T$ obtained by the improved pressure-correction formulation (blue lines) and by the modified pressure-correction formulation (red lines). The lines with dots refer to r_{10}, while the lines with triangles refer to r_{1000}. The dash-dotted line indicates second order convergence.

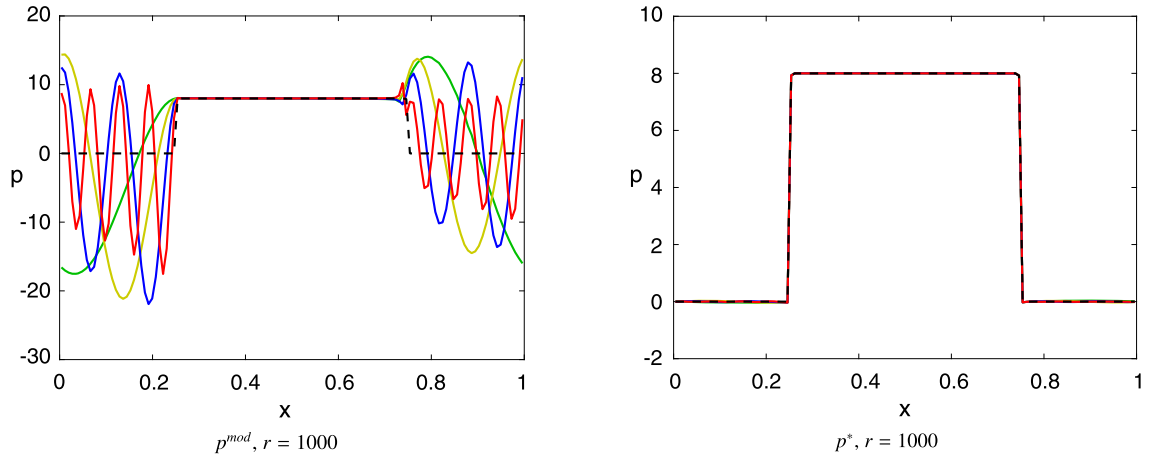

Fig. 9. Pressure profile in the centre line along the x-axis for CFL=0.32 (green line), CFL=0.16 (dark yellow line), CFL= 0.08 (blue line), CFL= 0.04 (red line) and for the reference solution (black dashed line) at $t = T$: p^{mod} (left figure); p^* (right figure). The density ratio is equal to 1000.

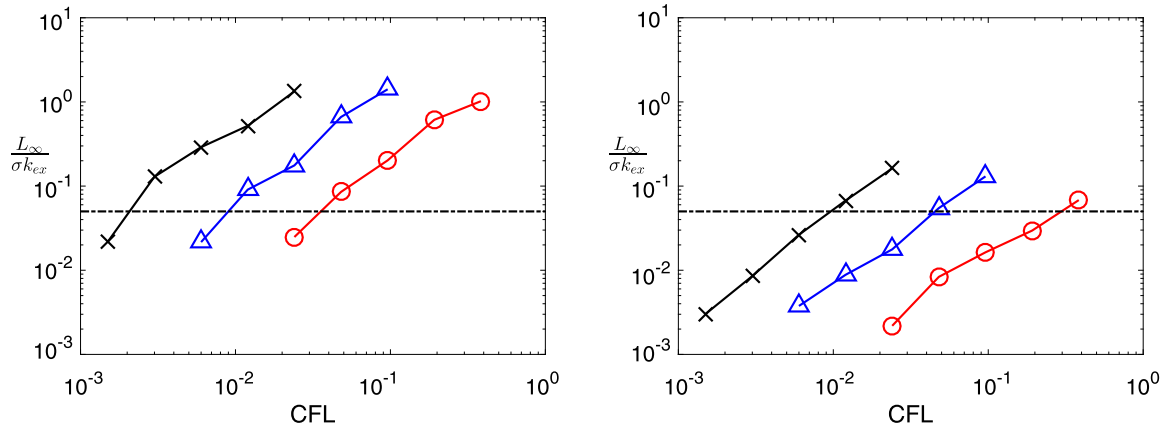

Fig. 10. L_∞ norm (38) scaled by the pressure jump σk_{ex} as a function of the CFL number for r_{10} (red line with circles), r_{100} (blue line with triangles) and r_{1000} (black line with crosses). The dash-dotted line indicates $\frac{L_\infty}{\sigma k_{ex}} = 5 \cdot 10^{-2}$. The left figure shows the error obtained for p^{mod}, the right figure shows the error obtained for p^*.

different density ratios: $r_{10} = 10$, $r_{100} = 10^2$, $r_{1000} = 10^3$. The numerical error is analysed as a function of the CFL number by considering a fixed grid resolution equal to 64^3 grid points. The parameters of the simulations are as follows: $\mu_l/\mu_g = 10$, $\mathrm{Eo} = \rho g d^2/\sigma = 10$ (Eötvös number) and $\mathrm{Mo} = g\mu^4/(\rho\sigma^3) = 6.7 \cdot 10^{-4}$ (Morton number), with d the bubble diameter. Apart from the varying density ratio, these parameters are the same as those used in [25] and also tested in [17], thus constituting a well established test case.

An initial uniform velocity field and periodic boundary conditions along the direction of gravity, have been prescribed. A sufficiently large CFL is realised such that the pressure jump extrapolation error becomes a relevant source of error. The latter is, in fact, negligible in the initial slow motion of a rising bubble, as observed in preliminary tests. Moreover, an additional source term has been introduced in the momentum equation in order to balance the weight of the mixture [26]. This test case should be therefore regarded as a prototype of developed flow conditions.

Extrapolation (3) may lead to unphysical oscillations of the pressure field when surface tension is present, as seen in Sec. 4.1. A measure of the wiggles intensity can be deduced by the L_∞ norm

$$L_\infty = \max |p_i - p_{\mathrm{ref},i}|. \tag{38}$$

In this subsection p_{ref} is the pressure field obtained by the unmodified pressure-correction formulation. Fig. 10 shows the norm (38) scaled by the exact pressure jump σk_{ex} as a function of the CFL number, for density ratios r_{10} (red line with circles), r_{100} (blue line with triangles) and r_{1000} (black line with crosses). Here k_{ex} is defined as the exact curvature of a spherical bubble occupying the same volume as the actual bubble. By a preliminary inspection of the results, the pressure profiles for which $\frac{L_\infty}{\sigma k_{ex}} \lessapprox 5 \cdot 10^{-2}$ were found not to show unphysical oscillations. This wiggle-free region is indicated by the lower part in the plots of Fig. 10 delimited by the dash-dotted horizontal line. The errors for p^* (right figure) are about

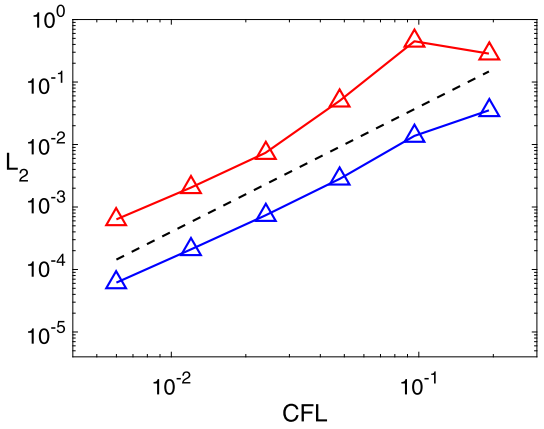

Fig. 11. L_2 norm of the pressure field as a function of the CFL number for $r = 100$. The blue line is the error for p^* and the red line is the error for p^{mod}. The dashed line indicates second order convergence.

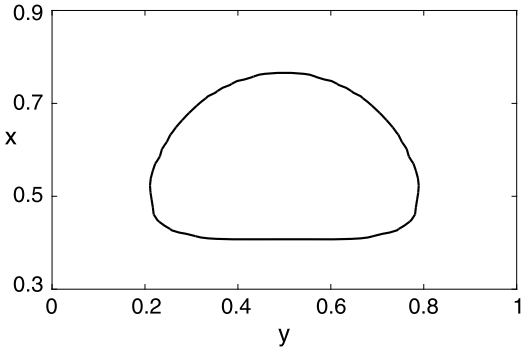

Fig. 12. Contour level $f = 0.5$ at the final time level for CFL=0.0125.

an order of magnitude smaller than those for p^{mod} (left figure). At a given density ratio an oscillation-free pressure field requires a value of CFL about 8 times smaller for p^{mod} than that required by p^*.

In Fig. 11 the convergence of the error with the CFL number is analysed by looking at the norm (37) for a fixed density ratio equal to 100. A varying CFL is realised by halving the value of the initial velocity field. Close to second order convergence is observed for both p^{mod} and p^*. Similar results were found for $r = 10, 1000$. A derivation of the scaling of pressure jump extrapolation error is provided in Appendix A.

The effect of the accumulation of the temporal truncation error is furthermore analysed. A longer simulation time, corresponding to about 30 cycles of the bubble throughout the domain, is considered. The parameters of the simulations are the same as those defined at the beginning of Sec. 4.2. The density ratio has been fixed to 100. Starting from CFL= 0.2, the time-step is halved until CFL= 0.0125 is reached. As an illustration, the final bubble shape for the smallest CLF is reported in Fig. 12. The pressure profiles on the centre line aligned with the direction of gravity (x-direction) are shown in Fig. 13 for p^{mod} (left figure) and for p^* (right figure). Both pressure p^{mod} and p^* show large oscillations at the largest CFL. However, the latter closely adhere to the reference pressure profile from CFL= 0.05 and smaller values. On the contrary, the former shows significant deviation from the reference solution also for the smallest simulated CFL. This is confirmed by the L_2 norm of the error in the pressure field shown in Fig. 14. Close to first order convergence is recovered by p^*. This is attributed to the fact that the temporal truncation error of pressure also depends on the temporal accuracy of the term $\tilde{D}(\tilde{\mathbf{u}}^*)/\Delta t$ [2]. The latter is by construction an order of accuracy lower than the temporal accuracy of the velocity field. Thus, it brings about a contribution $\mathcal{O}(\Delta t)$ in contrast to $\mathcal{O}(\Delta t^2)$ of (28). Pressure p^{mod} shows a convergence rate of approximately 1.4, indicating that the contribution of the pressure extrapolation error to the total error is still comparable with the lower order temporal accuracy related to the term $\widetilde{\mathcal{D}}(\tilde{\mathbf{u}}^*)/\Delta t$.

Having analysed the accuracy of pressure, the attention is now turned to velocity. Numerically, the effect of the pressure gradient on the velocity field appears in the final step of the projection method. Taking into account the surface tension contribution, the correction to the velocity field (10) in the unmodified pressure-correction formulation reads:

$$\left(\frac{1}{\rho}\left(\mathcal{G}p - \sigma k \mathcal{G} f\right)\right)^{n+1}. \tag{39}$$

Analogously, the correction to the velocity field (13) in the modified pressure-correction formulation is

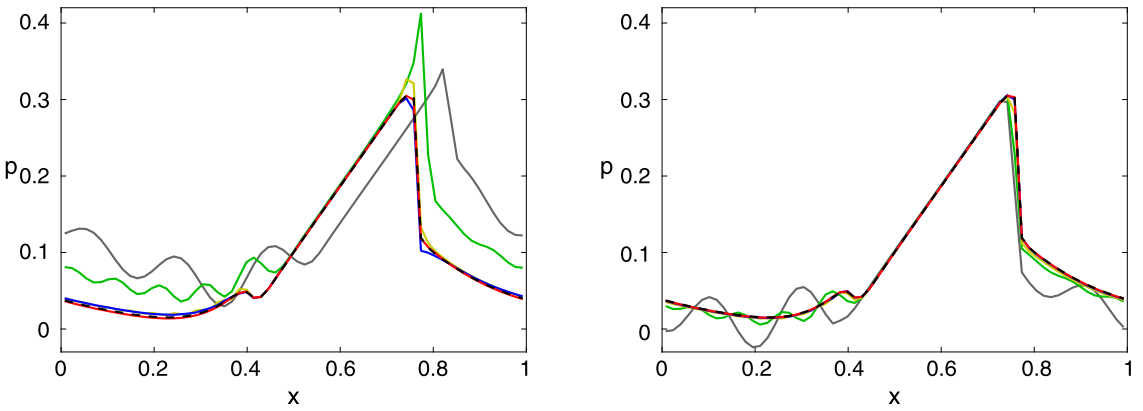

Fig. 13. Pressure profile along x of p^{mod} (left figure) and of p^* (right figure) for different Δt corresponding to the following CFL numbers: CFL= 0.2 (grey line), CFL= 0.1 (green line), CFL= 0.05 (dark-yellow line), CFL= 0.025 (blue line) and CFL= 0.0125 (red line). The pressure field obtained by using the unmodified pressure-correction formulation at CFL= 0.0125 is reported by the black dashed line.

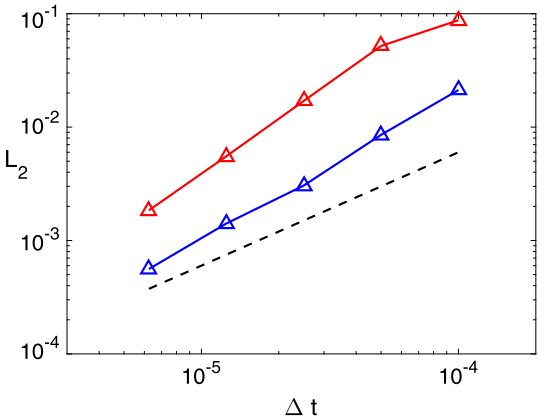

Fig. 14. L_2 norm of the pressure field error as a function of Δt at the final time for p^* (blue lines with triangles) and for p^{mod} (red lines with triangles). The dashed line indicates first order convergence.

$$\frac{1}{\rho_0}\mathcal{G}p^{n+1} + \left(\frac{1}{\rho^{n+1}} - \frac{1}{\rho_0}\right)\mathcal{G}\hat{p} - \left(\frac{1}{\rho}\sigma k \mathcal{G} f\right)^{n+1}, \tag{40}$$

and the correction to the velocity field (35) in the improved pressure-correction formulation is

$$\frac{1}{\rho_0}\left(\mathcal{G}p^{n+1} - (\sigma k \mathcal{G} f)^{n+1}\right) + \left(\frac{1}{\rho^{n+1}} - \frac{1}{\rho_0}\right)\left(\mathcal{G}\hat{p} - \widehat{\sigma k \mathcal{G} f}\right). \tag{41}$$

Corrections (39) and (41) only contain an approximation of the smooth pressure gradient. This is the result of having combined the pressure gradient with the volume fraction gradient, as in (32). In contrast, correction (40) contains a mixed contribution from the jump at time level $n+1$ and the extrapolated pressure gradient. The modified pressure-correction formulation will then lead to larger errors in the velocity field than those related to the improved pressure-correction formulation. This is qualitatively shown in Fig. 15. The velocity profiles along x at the final time are reported for different Δt. The profile at the smallest Δt tends to overlap with the reference solution. Nevertheless, the velocity field obtained from p^* shows a significantly more accurate prediction for the larger Δt.

Finally, Fig. 16 shows the L_2 norm of the error of the velocity field obtained from p^* (blue line with triangles) and from p^{mod} (red line with triangles). Second order accuracy is achieved by the improved pressure-correction formulation, as expected from theory. The modified pressure-correction formulation presents larger errors at the larger Δt analysed. However, no significant difference is observed from a Δt corresponding to CFL= 0.05 and lower values. This is consistent with the fact that the pressure gradient corrections (39)–(41) appear in the momentum equation multiplied by a factor Δt. Hence, the difference between the two pressure-correction formulations will decrease faster in the velocity field than in the pressure field as Δt is reduced.

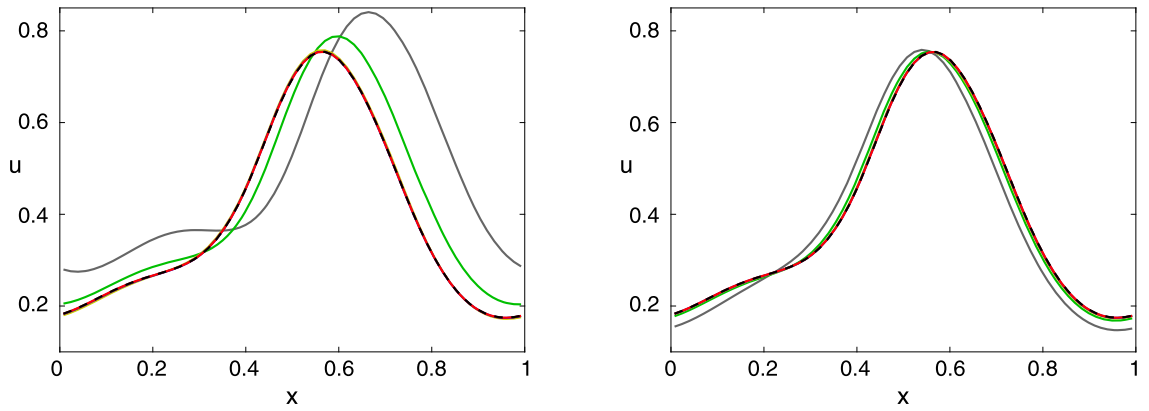

Fig. 15. Velocity profile along x obtained from the modified pressure-correction formulation (left figure) and from the improved pressure-correction formulation (right figure), for different Δt corresponding to the following CFL numbers: CFL= 0.2 (grey line), CFL= 0.1 (green line), CFL= 0.05 (dark-yellow line), CFL= 0.025 (blue line) and CFL= 0.0125 (red line). The velocity profile obtained by employing the unmodified pressure-correction formulation at CFL= 0.0125 is reported by the black dashed line.

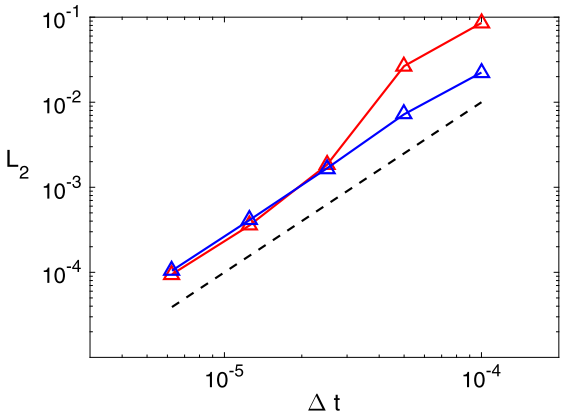

Fig. 16. L_2 norm of the velocity field error at the final time as a function of Δt for the improved pressure-correction formulation (blue lines with triangles) and for the modified pressure-correction formulation (red lines with triangles). The dashed line indicates second order convergence.

5. Conclusions

A thorough analysis of the modified pressure-correction formulation, originally developed by [5], was carried out. By means of a temporal extrapolation of the pressure gradient, the pressure equation can be reduced to a constant-coefficient Poisson equation, for which efficient linear solvers can be used. While the gain in speed-up is well documented, the accuracy of such method has been largely overlooked. The goal of this paper is to provide a detailed quantification of the pressure extrapolation error. This analysis will constitute a point of reference when designing fast Poisson solvers for fully resolved two-phase flows. As it becomes clear from this work, the extrapolation in time of the pressure gradient can lead to unphysical oscillations, which severely deteriorate the numerical solution of the problem. While an improved pressure-correction formulation is able to significantly reduce the pressure oscillations, the error brought about by the temporal extrapolation of pressure is, in general, non-negligible. The convergence study presented here will thus serve as a guideline for the choice of grid size and time step.

The origin of the numerical pressure oscillations was found to be the result of a straightforward application of extrapolation (3) to the pressure field in the presence of a discontinuity, namely the surface tension jump. A grid convergent pressure field could be achieved by combining the extrapolated pressure gradient with a corresponding volume fraction gradient, as expressed by (32). In the case of constant curvature, the latter procedure delivers an exact balance between pressure and surface tension. Furthermore, in the general case of non-constant curvature, relation (32) constitutes an approximation of the smooth part of the pressure gradient, which can be accurately approximated by extrapolation (3) where smoothness is assumed. The resulting formulation, embedded in the steps of the projection method (33), (34), (35), allows to greatly reduce the error values in the pressure field up to an order of magnitude lower than those obtained by the modified pressure-correction formulation (8), (12), (13).

The analysis of the one-dimensional prototype problem (Sec. 3.2) was carried out with the twofold aim of showing the origin of spurious pressure oscillations and of detailing the property a numerical scheme should have in order to mimic the

physics of a moving front. The source of numerical inconsistency has been traced back to a poor extrapolation of the jump condition in the pressure field from previous time levels (Sec. 3.2.4), which leads to the appearance of pressure wiggles regardless of the grid size and of the time step of the simulation. The improved pressure-correction formulation, illustrated in Sec. 3.2.5, allowed to recover the exact solution for this problem.

A translating sphere was then simulated in Sec. 4.1, for a density ratio of 10 and 1000. Second order accuracy and an essentially wiggle-free pressure field is achievable by using the improved pressure-correction formulation, while the modified pressure-correction formulation led to large pressure oscillations and failed to converge upon grid refinement. This confirmed the findings obtained in the simplified one-dimensional problem analysed in Sec. 3.2.

In Sec. 4.2 the full problem, comprising of the Navier-Stokes equations, was analysed for a rising bubble in an upflow. Numerical tests on the L_2 norm showed that pressure p^*, obtained by the improved pressure-correction formulation, is about an order of magnitude more accurate for all the simulated density ratios. At a given density ratio an oscillation-free pressure field requires a value of CFL about 8 times smaller for the pressure obtained by the modified pressure-equation formulation p^{mod} than that required for the pressure obtained by the improved pressure-equation formulation p^*. An approximately quadratic dependence of the pressure jump extrapolation error on the CFL number was found.

The accumulation of the temporal truncation error was then analysed, for the same case of a rising bubble, at density ratio equal to 100. Both p^{mod} and p^* showed spurious oscillations for the larger time steps considered. However, a significantly smaller error was observed for p^* at the smaller and intermediate values of the time step where an oscillation-free pressure field could be recovered. For a given Δt, the effect of the pressure extrapolation error on the velocity field was found to be smaller than that on the pressure field. This is consistent with the higher temporal accuracy of $\mathbf{u}$ compared to p.

Besides its mere kinematic role to enforce continuity, pressure is also a fundamental quantity for the computation of fluid-dynamic forces, as for example in fluid-structure interaction problems [27,28]. Furthermore, DNS databases are analysed as a source from which to extract physical insights for deriving averaged equation models [1]. An accurate computation of pressure becomes then crucial.

As a final remark, the use of the modified pressure-correction formulation is only worthwhile when the additional computational time the reduction of the pressure extrapolation error may require is lower than the gain in computational time provided by fast Poisson solvers.

Declaration of competing interest

The authors declare that they have no known competing financial interests or personal relationships that could have appeared to influence the work reported in this paper.

Acknowledgements

The Netherlands Organization for Scientific Research (NWO) is gratefully acknowledged for granting access to national supercomputer facilities. This work was carried out on the Dutch national e-infrastructure with the support of SURF Cooperative. Furthermore, I wish to thank prof. dr. A.E.P. Veldman for the valuable suggestions that helped to improve the quality of this paper.

Appendix A

In order to show the influence of the CFL number on the pressure jump extrapolation error, the one-dimensional moving front detailed in Sec. 3.2 is considered. Substitution of the analytical solution (17) into the semi-discrete modified pressure equation (2) yields:

$$\frac{\partial^2 f^{n+1}}{\partial x^2} = \frac{\partial}{\partial x}\left[\left(1-\frac{\rho_g}{\rho}\right)\frac{\partial \hat{f}}{\partial x}\right] + \frac{\partial}{\partial x}\left(\rho_g \frac{\mathbf{u}^*}{\alpha \Delta t}\right), \tag{A.1}$$

where, according to extrapolation (3), $\hat{f} = 2f^n - f^{n-1}$. Note, here $\rho_0 = \rho_g$ as discussed in Sec. 3.2.3. Differentiation of Eq. (6) with respect to time leads to

$$\frac{\partial^2 f}{\partial t^2} = -U\frac{\partial^2 f}{\partial t \partial x} = U^2 \frac{\partial^2 f}{\partial x^2}, \tag{A.2}$$

where is the last step Eq. (6) has been used once more. While in the derivations carried out in Sec. 3.2 the advection of f was assumed to be exact, here the error due to the time marching of f is analysed by introducing a discretisation scheme for the temporal derivative. In particular, an Euler forward scheme is employed. Under this assumption, Eq. (A.2) is discretised as

$$\frac{f^{n+1} - 2f^n + f^{n-1}}{\Delta t^2} = U^2 \frac{\partial^2 f^{n-1}}{\partial x^2}, \tag{A.3}$$

from which $\hat{f}$ can be obtained:

$$\hat{f} = f^{n+1} - (U\Delta t)^2 \frac{\partial^2 f^{n-1}}{\partial x^2}. \tag{A.4}$$

Substitution of (A.4) into (A.1) yields

$$\frac{\partial}{\partial x}\left(\frac{1}{\rho}\frac{\partial f^{n+1}}{\partial x}\right) = -(U\Delta t)^2 \frac{\partial}{\partial x}\left[\left(\frac{1}{\rho_g} - \frac{1}{\rho}\right)\frac{\partial^3 f^{n-1}}{\partial x^3}\right] + \frac{\partial}{\partial x}\left(\frac{\mathbf{u}^*}{\alpha\Delta t}\right). \tag{A.5}$$

Analogously, Eq. (1) reduces to:

$$\frac{\partial}{\partial x}\left(\frac{1}{\rho}\frac{\partial f^{n+1}}{\partial x}\right) = \frac{\partial}{\partial x}\left(\frac{\mathbf{u}^*}{\alpha\Delta t}\right). \tag{A.6}$$

The first term in the RHS of (A.5) can be further reduced by considering the case of a liquid cell ($\rho = \rho_l$) close to a moving interface. In a neighbouring gas cell the quantity between square brackets, indicated by $[\cdot]$, is zero since $\rho = \rho_g$. Hence, a finite difference approximation of $\partial[\cdot]/\partial x$ will be approximately equal to $[\cdot]/\Delta x$. Similarly, derivatives $\partial^q f/\partial x^q$, across the interface, will be approximated by finite differences of order $1/\Delta x^q$. Finally, by first multiplying Eqs. (A.5), (A.6) by the mesh size squared and subsequently subtracting Eq. (A.5) from Eq. (A.6), an estimate of the pressure jump extrapolation error is found:

$$E_\sigma = \mathcal{O}\left[\left(\frac{1}{\rho_g} - \frac{1}{\rho_l}\right) CFL^2\right]. \tag{A.7}$$

Despite the simplifying assumptions used to derive relation (A.7), error E_σ appears to well predict the scaling of the pressure error numerically analysed in Fig. 11.

References

[1] A. Prosperetti, G. Tryggvason, Computational Methods for Multiphase Flow, Cambridge University Press, 2007.
[2] M.J. Lee, B. Do Oh, Y.B. Kim, Canonical fractional-step methods and consistent boundary conditions for the incompressible Navier–Stokes equations, J. Comput. Phys. 168 (2001) 73–100.
[3] P. Wesseling, Introduction to multigrid methods, 1995.
[4] T.F. Chan, W.L. Wan, Robust multigrid methods for nonsmooth coefficient elliptic linear systems, J. Comput. Appl. Math. 123 (2000) 323–352.
[5] S. Dong, J. Shen, A time-stepping scheme involving constant coefficient matrices for phase-field simulations of two-phase incompressible flows with large density ratios, J. Comput. Phys. 231 (2012) 5788–5804.
[6] M.S. Dodd, A. Ferrante, A fast pressure-correction method for incompressible two-fluid flows, J. Comput. Phys. 273 (2014) 416–434.
[7] X.-D. Liu, R.P. Fedkiw, M. Kang, A boundary condition capturing method for Poisson's equation on irregular domains, J. Comput. Phys. 160 (2000) 151–178.
[8] M. Sussman, K.M. Smith, M.Y. Hussaini, M. Ohta, R. Zhi-Wei, A sharp interface method for incompressible two-phase flows, J. Comput. Phys. 221 (2007) 469–505.
[9] J. Yang, F. Stern, Sharp interface immersed-boundary/level-set method for wave–body interactions, J. Comput. Phys. 228 (2009) 6590–6616.
[10] Z. Ge, J.-C. Loiseau, O. Tammisola, L. Brandt, An efficient mass-preserving interface-correction level set/ghost fluid method for droplet suspensions under depletion forces, J. Comput. Phys. 353 (2018) 435–459.
[11] C.W. Hirt, B.D. Nichols, Volume of fluid (VOF) method for the dynamics of free boundaries, J. Comput. Phys. 39 (1981) 201–225.
[12] M. Sussman, P. Smereka, S. Osher, A level set approach for computing solutions to incompressible two-phase flow, J. Comput. Phys. 114 (1994) 146–159.
[13] S.O. Unverdi, G. Tryggvason, A front-tracking method for viscous, incompressible, multi-fluid flows, J. Comput. Phys. 100 (1992) 25–37.
[14] M. Sussman, E.G. Puckett, A coupled level set and volume-of-fluid method for computing 3D and axisymmetric incompressible two-phase flows, J. Comput. Phys. 162 (2000) 301–337.
[15] J.U. Brackbill, D.B. Kothe, C. Zemach, A continuum method for modeling surface tension, J. Comput. Phys. 100 (1992) 335–354.
[16] P. Cifani, J.G. Kuerten, B.J. Geurts, Highly scalable DNS solver for turbulent bubble-laden channel flow, Comput. Fluids 172 (2018) 67–83.
[17] P. Cifani, W.R. Michalek, G.J.M. Priems, J.G.M. Kuerten, C.W.M. van der Geld, B.J. Geurts, A comparison between the surface compression method and an interface reconstruction method for the VOF approach, Comput. Fluids 136 (2016) 421–435.
[18] S. Popinet, An accurate adaptive solver for surface-tension-driven interfacial flows, J. Comput. Phys. 228 (2009) 5838–5866.
[19] R.W.C.P. Verstappen, A.E.P. Veldman, Symmetry-preserving discretization of turbulent flow, J. Comput. Phys. 187 (2003) 343–368.
[20] M.M. Francois, S.J. Cummins, E.D. Dendy, D.B. Kothe, J.M. Sicilian, M.W. Williams, A balanced-force algorithm for continuous and sharp interfacial surface tension models within a volume tracking framework, J. Comput. Phys. 213 (2006) 141–173.
[21] S. Popinet, Numerical models of surface tension, Annu. Rev. Fluid Mech. 50 (2018) 1–28.
[22] T. Ménard, S. Tanguy, A. Berlemont, Coupling level set/VOF/ghost fluid methods: validation and application to 3D simulation of the primary break-up of a liquid jet, Int. J. Multiph. Flow 33 (2007) 510–524.
[23] S.J. Cummins, M.M. Francois, D.B. Kothe, Estimating curvature from volume fractions, Comput. Struct. 83 (2005) 425–434.
[24] P. Wesseling, Principles of Computational Fluid Dynamics, Vol. 29, Springer Science & Business Media, 2009.
[25] S. Hysing, S. Turek, D. Kuzmin, N. Parolini, E. Burman, S. Ganesan, L. Tobiska, Quantitative benchmark computations of two-dimensional bubble dynamics, Int. J. Numer. Methods Fluids 60 (2009) 1259–1288.
[26] J. Lu, S. Biswas, G. Tryggvason, A DNS study of laminar bubbly flows in a vertical channel, Int. J. Multiph. Flow 32 (2006) 643–660.
[27] J. Degroote, Partitioned simulation of fluid-structure interaction, Arch. Comput. Methods Eng. 20 (2013) 185–238.
[28] M.D. de Tullio, G. Pascazio, A moving-least-squares immersed boundary method for simulating the fluid-structure interaction of elastic bodies with arbitrary thickness, J. Comput. Phys. 325 (2016) 201–225.